Article

Label-free bio-aerosol sensing using mobile microscopy and deep learning

Yichen Wu, Ayfer Calis, Yi Luo, Cheng Chen, Maxwell Lutton, Yair Rivenson, Xing Lin, Hatice Ceylan Koydemir, Yibo Zhang, Hongda Wang, Zoltán Göröcs, and Aydogan Ozcan

ACS Photonics, **Just Accepted Manuscript** • DOI: 10.1021/acsphotonics.8b01109 • Publication Date (Web): 04 Oct 2018

Label-free bio-aerosol sensing using mobile microscopy and deep learning

Yichen Wu,[1,2,3] Ayfer Calis,[1,2,3] Yi Luo,[1,2,3] Cheng Chen,[1] Maxwell Lutton,[4] Yair Rivenson,[1,2,3] Xing Lin,[1,2,3] Hatice Ceylan Koydemir,[1,2,3] Yibo Zhang,[1,2,3] Hongda Wang,[1,2,3] Zoltán Göröcs,[1,2,3] Aydogan Ozcan,[1,2,3,5,*]

[1]Electrical and Computer Engineering Department, University of California, Los Angeles, California 90095, USA

[2]Bioengineering Department, University of California, Los Angeles, California 90095, USA

[3]California NanoSystems Institute (CNSI), University of California, Los Angeles, California 90095, USA

[4]Computer Science Department, University of California, Los Angeles, California 90095, USA

[5]Department of Surgery, David Geffen School of Medicine, University of California, Los Angeles, California 90095, USA

[*]Corresponding author: ozcan@ucla.edu

KEYWORDS: deep learning, label-free sensing, air quality, aerosol, computational microscopy, digital holography

ABSTRACT: Conventional bio-aerosol sensing requires the sampled aerosols in the field to be transferred to a laboratory for manual inspection, which can be rather costly and slow, also requiring a professional for labeling and microscopic examination of the samples. Here we demonstrate label-free bio-aerosol sensing using a field-portable and cost-effective device based on holographic microscopy and deep-learning, which screens bio-aerosols at a throughput of 13 L/min. Two different deep neural networks are designed to rapidly reconstruct the amplitude and phase images of the captured bio-aerosols, and to classify the type of each bio-aerosol that is imaged. As a proof-of-concept, we studied label-free sensing of common bio-aerosol types, e.g., Bermuda grass pollen, oak tree pollen, ragweed pollen, Aspergillus spore, and Alternaria spore and achieved >94% classification accuracy. The presented label-free bio-aerosol measurement device, with its mobility and cost-effectiveness, will find several applications in indoor and outdoor air quality monitoring.

A human adult inhales about seven liters of air every minute, which on average contains 10^2-10^3 micro-biological cells (bio-aerosols) [1,2]. In some contaminated environments, this number can easily exceed 10^6 [1,3–5]. These bio-aerosols are micro-scale airborne living organisms that originate from plants or animals, and include pollens, mold/fungi spores, bacteria, and viruses. They are generated both naturally and anthropogenically, from e.g. animal houses [6,7], composting facilities [6,7], and construction sites [7]. These bio-aerosols can stay suspended in the air for prolonged periods of time [6], remain at significant concentrations even far away from the generating site (up to one kilometer) [8–10], and can travel through continental distances [11]. Basic environmental conditions, such as temperature and moisture level, can also considerably influence bio-aerosol formation and dispersion [7,12]. Inhaled by a human, they can stay in the respiratory tract and cause irritation, allergies, various diseases including cancer and even premature death [1,2,6,7,10,11,13–15]. In fact, bio-aerosols account for 5-34% of indoor particulate matter (PM) [16]. In recent years, there has been increased interest in monitoring environmental bio-aerosols, and understanding their composition, to avoid and/or mitigate their negative impacts on human health [1,7,17,18], in both peacetime and in threat of biological attacks [15].

Currently, most of the bio-aerosol monitoring activities still rely on a technology that was developed more than fifty years ago [7,19,20]. In this method, an aerosol sample is taken in the inspection site using a sampling device such as an impactor, a cyclone, a filter, or a spore trap. This sample is then transmitted to a laboratory, where the aerosols are transferred to certain liquid media or solid substrates and inspected manually under a microscope or through culture experiments. The microscopic inspection of the sample usually involves labeling through a colorimetric or fluorescence stain to increase the contrast of the captured bio-aerosols under a microscope [21,22]. Regardless of the specific method that is employed, the use of manual inspection in a laboratory, following a field collection, significantly increases the costs and delays the reporting time of the results. Partially due to these limitations, out of ~10,000 air-sampling stations worldwide, only a very small portion of them have bio-aerosol sensing/measurement capability. Even in developed countries, bio-aerosol levels are only reported on a daily basis at city scales [23]. As a result, human exposure to bio-aerosols is hard to quantify with the existing set of technologies.

Driven by this need, different techniques have been emerging towards potentially label-free, on-site and/or real-time bio-aerosol monitoring. In one of these techniques, the air is driven through a small channel, and an ultraviolet (UV) source is focused on a nozzle of this channel, exciting the auto-fluorescence of each individual bio-aerosol flowing through the nozzle [24–28]. This auto-fluorescence signal is then captured by one or more photodetectors, used to differentiate bio-aerosols from non-fluorescent background aerosols. Recently, other machine learning algorithms have also been applied to classify bio-

aerosols from their auto-fluorescence signals[27,28] (see Supplementary Materials for details). However, measuring auto-fluorescence in itself may not provide sufficient specificity towards classification. To detect weak auto-fluorescence signals, this design also requires strong UV sources, sensitive photodetectors and high-performance optical components, making the system relatively costly and bulky. Furthermore, the sequential read-out scheme in these flow-based designs also limits their sampling rate and throughput to < 5 L/min. Alternative bio-aerosol detection methods rely on anti-bodies to specifically capture bio-aerosols of interest on e.g., a vibrational cantilever [29,30], or a surface plasmon resonance (SPR) substrate [17,31], which can then detect these captured bio-aerosols through a change in the cantilever vibrational frequency or a shift in the SPR spectrum, respectively. These approaches provide very sensitive detection of a specific type of bio-aerosols. However, their performance can be compromised by non-specific binding and/or changes in the environmental conditions (e.g., temperature, moisture level etc.), impacting the effectiveness of the surface chemistry. Moreover, the reliance to specific antibodies makes it harder for these approaches to scale up the number of target bio-aerosols and cover unknown targets. Bio-aerosol detection and composition analysis using Raman spectroscopy has also been demonstrated [32,33]. However, due to weaker signal levels and contamination from background spectra, the sensitivities of these methods have been relatively low despite their expensive and bulky hardware; it is challenging to analyze or detect e.g., a single bio-aerosol within a mixture of other aerosols. It is also possible to detect bio-aerosols by detecting their genetic material (e.g., DNA), using polymerase chain reaction (PCR) [34], enzyme-linked immunosorbent assays (ELISA) [35] or metagenomics [36,37], all of which can provide high sensitivity and specificity. However, these detection methods are usually based on post-processing of bio-aerosols in laboratory environments (i.e., involves field sampling, followed by the transportation of the sample to a central laboratory for advanced processing), and are therefore low-throughput, also requiring an expert. Therefore, there is still an urgent unmet need for accurate, label-free and automated bio-aerosol sensing to cover a wide range of bio-aerosols, ideally within a field-portable, compact and cost-effective platform.

To address this need, we developed a high-throughput and mobile bio-aerosol detection system based on computational microscopy and deep learning (Figure 1). Our device design uses a combination of an impactor and a lensless digital holographic on-chip microscope [38–42]: bio-aerosols in air are captured on the impactor substrate at a sampling rate of 13 L / min. These collected bio-aerosols generate diffraction holograms recorded directly by an image sensor chip that is positioned right below the substrate. Each hologram contains information of the complex optical field, and therefore both the amplitude and phase information of each individual bio-aerosol are captured. After digital holograms of bio-aerosols are acquired and transmitted to a remote server (which can also be a local PC), these holograms are rapidly processed through an image-processing pipeline (Figure 2), within a minute, reconstructing the entire field-of-view (FOV) of our device, i.e., 4.04 mm^2, over which the captured bio-aerosols are analyzed. Enabled by deep convolutional neural networks (CNNs) [43], this reconstruction algorithm first reconstructs both the amplitude and phase image of each individual bio-aerosol with sub-micron resolution, and then performs automatic classification of the imaged bio-aerosols into pre-trained classes and counting the density of each class in air. To show the proof-of-concept of our device, we demonstrate the reconstruction and label-free sensing of five different types of bio-aerosols: Bermuda grass pollen, oak tree pollen, ragweed pollen, Aspergillus spore, and Alternaria spore – as well as non-biological aerosols as part of the default background pollution. The Bermuda grass, oak tree and ragweed pollens have long been recognized as some of the most common grass, tree and weed-based allergens that can cause severe allergic reactions [11,44–46]. Similarly, the Aspergillus and Alternaria spores are two of the most common mold spores found in air [1,3–5,9] and can cause allergic reactions and various diseases [6,7,10,11]. Furthermore, Aspergillus spores have been proven to be a culprit of asthma in children [6]. Some of these mold species/sub-species can also generate mycotoxins that weaken the human immune system [7]. In this work, a deep CNN is trained to differentiate these six different types of aerosols, achieving an accuracy of 94% using our mobile instrument. This label-free bio-sensing platform can be further scaled up to specifically detect other types of bio-aerosols by training it using purified populations of new target object types as long as these bio-aerosols exhibit unique spatial and/or spectral features that can be detected through our holographic imaging system.

To the best of our knowledge, this is the first demonstration of automated label-free sensing and classification of bio-aerosols using a portable and cost-effective device, which is enabled by computational microscopy and deep-learning, which we use for both image reconstruction and particle classification. The presented mobile bio-aerosol detection device is hand-held, weighs less than 600 g, and its parts cost less than $200 under low-volume manufacturing. Compared to our earlier results on PM measurements using mobile microscopy without any classification capability,[38] this work reports label-free and automated bio-aerosol sensing using deep learning (which is used for both image reconstruction and classification), providing a unique capability for specific and sensitive detection and counting of e.g., pollen and mold particles in air. We believe the presented platform can find a wide range of applications in label-free bio-aerosol sensing and environmental monitoring.

RESULTS AND DISCUSSION

Quantification of spatial resolution and field-of-view

A USAF-1951 resolution test target is used to quantify the spatial resolution of our device. Figure S1 shows the reconstructed image of this test target, where the smallest resolvable line is group nine, element one (with a line width of 0.98 μm), which in this case is limited by the pixel pitch of the image sensor chip (1.12 μm). Compared to our earlier work[38], this resolution is improved by two-fold owing to higher coherence of the laser diode, a smaller pixel pitch of the image sensor (1.12 μm), and using all four Bayer channels of the color image sensor chip under 850

nm illumination, where an RGB image sensor behaves similar to a monochrome sensor. For the current bio-aerosol sensing application, this resolution provides accurate detection performance, revealing the necessary spatial features of the particles in both the phase and amplitude image channels, as will be detailed in subsequent sub-sections. In case future applications require better spatial resolution to reveal even finer spatial structures of some target bio-aerosols, the resolution of our platform can be further improved by using an image sensor chip with a smaller pixel pitch, and/or by applying pixel super-resolution techniques that can digitally achieve an effective pixel < 0.5 μm [47–49].

In our device design, the image sensor chip has an active area of $3.674\ mm \times 2.760\ mm = 10.14\ mm^2$, which would normally be the sample FOV for a lens-less on-chip microscope. However, our imaging FOV is smaller than this because the sampled aerosols deposit directly below the impaction nozzle, thus the active FOV of our mobile instrument is defined by the overlapping area of the image sensor chip and the impactor nozzle, which results in an effective FOV of $3.674\ mm \times 1.1\ mm = 4.04\ mm^2$. This FOV can be further increased up to the active area of the imager chip by customizing the impactor design with a larger nozzle width.

Label-free bio-aerosol image reconstruction

For each bio-aerosol measurement, two holograms are taken (before and after sampling the air) by our mobile device, and their per-pixel difference is calculated forming a differential hologram (see Supplementary Materials for details) [50,51]. This differential hologram is numerically back-propagated in free space by an axial distance of ~750 μm to roughly reach the object plane of the sampling surface (see Methods and Supplementary Materials for details). This axial propagation distance does not need to be precisely known, and in fact all the aerosols within this back-propagated image are automatically autofocused and phase recovered at the same time using a deep neural network that was trained with out-of-focus holograms of particles (within +/-100 μm of their corresponding axial position) to extend the depth-of-field (DOF) of our reconstructions (see e.g., Figure S2) [43]. This feature of the neural net is extremely beneficial to speed up auto-focusing and phase recovery steps since it reduces the computational complexity of our reconstructions from $O(n{\cdot}m)$ to $O(1)$, where n refers to the number of aerosols within our FOV and m refers to the axial search range that would have been used for auto-focusing each particle using classical holographic reconstruction methods that involve phase recovery. In this regard, deep learning is crucial to rapidly reconstruct and auto-focus each bio-aerosol's phase and amplitude image using our mobile device.

To illustrate the reconstruction performance of this method, Figure 3 shows the raw holograms, back-propagation and neural network results corresponding to six different cropped region-of-interests (ROIs), one for each of the six classes used in this paper (Bermuda grass pollen, oak tree pollen, ragweed pollen, Alternaria mold spores, Aspergillus mold spores, and generic dust). The propagation distance (750 μm) is not exact for all these particles, which would normally result in de-focused images. This defocus is corrected automatically by our trained neural network, as shown in Figure 3(c). In addition, the twin-image and self-interference artifacts of holographic imaging (e.g., the ripples at the background of Figure 3(b); also see Supplementary Materials for details) are also eliminated in Figure 3(c), demonstrating phase-recovery in addition to auto-focusing on each captured particle. Microscope comparisons captured under a 20× objective (NA=0.75) with a 2× adapter are also shown for the same six ROIs (Figure 3(d)).

The neural network output (Figure 3(c)) clearly illustrates the morphological differences among these different aerosols, in both the real and imaginary channels of the reconstructed images, providing unique features for classification of these aerosols, as will be discussed in the next sub-section.

Bio-aerosol image classification

A separate CNN is developed that takes a cropped ROI (after the image reconstruction and auto-focusing step detailed earlier) and automatically assigns one of the six class labels for each detected aerosol (see Figure 2 and Methods for details). Table 1 reports the classification precision and recall on the testing set, as well as their harmonic mean, known as F-number (F#), which are defined as:

$$\text{Precision} = \frac{\text{True Positive}}{\text{True Positive} + \text{False Positive}} \quad (1)$$

$$\text{Recall} = \frac{\text{True Positive}}{\text{True Positive} + \text{False Negative}} \quad (2)$$

$$\text{F\#} = \frac{2 \cdot \text{Precision} \cdot \text{Recall}}{\text{Precision} + \text{Recall}} \quad (3)$$

As shown in Table 1, an average precision of ~94.0%, and an average recall of ~93.5% are achieved for the six labels using this classification CNN for a total number of 1,391 test particles that were imaged by our instrument. In Table 1, we see that the classification performance of our mobile device is relatively lower for Aspergillus spores compared to other classes. This is due to the fact that (1) Aspergillus spores are smaller in size (~ 4 μm), so their fine features may not be well-revealed under the current imaging system resolution, and (2) the Aspergillus spores sometimes cluster and may exhibit a different shape compared to an isolated spore (for which the network was trained for). In addition to these, the background dust images used in our testing are captured along the major roads with traffic. Although it should contain mostly non-biological aerosols, there is a finite chance that a few bio-aerosols may also be present in our data set, leading to mislabeling.

Table 1 also compares the performance of two other classification methods on the same data set, namely AlexNet [52] and support vector machine (SVM) [53] (see Supplementary Material for details). AlexNet, although has more trainable parameters in the network design (because of the larger fully connected layers), performs ~1.8% worse in precision and 1.2% worse in recall compared to the CNN developed in this work. SVM, although very fast to

compute, has significantly worse performance than our CNN models, reaching only 78.1% precision and 73.2% recall on average for our testing set.

Bio-aerosol mixture experiments

To further quantify the label-free sensing performance of our platform, we did two additional sets of experiments – one with a mixture of the three pollens, and another with a mixture of the two mold spores. In addition, in each experiment there were also unavoidably dust particles (background PM) other than the pollens and mold spores that were introduced into our device and were sampled and imaged on the detection substrate.

To quantify the performance of our device, the sampled sticky substrate in each experiment was also examined (after our lens-less imaging) by a microbiologist under a scanning microscope with 40× magnification, where the corresponding FOV that was analyzed by our mobile device was scanned and the captured bio-aerosols inside each FOV were manually labeled and counted by a microbiologist (for comparison purposes). The results of this comparison are shown in Figure 4(a-f), where Figure 4(a-d) is from four independent pollen mixture experiments and Figure 4(e,f) is from two independent mold spores mixture experiments. The confusion matrix for each sample is also shown in Figure S3.

To further quantify our detection accuracy, Figure 4(g-l) plots the results of Figure 4(a-f) individually for each of the six classes, where the x-axis is the manual count made by an expert and the y-axis is the automatic count generated by our mobile device. In these results, we observe a relatively large overcounting for Alternaria and undercounting for Aspergillus in Figure 4(e,f), as also seen by their larger root mean square error (RMSE). This may be related to the fact that (1) the mold spores are smaller and therefore relatively more challenging to classify using the current resolution of our system, and (2) the mold spores tend to coagulate due to moisture, which may confuse the CNN model when they are present in the same ROI (see e.g., Figure S4). These results might be further improved using per-pixel semantic segmentation [54] instead of performing classification with a fixed window size.

Field sensing of oak tree pollens

We also demonstrated the detection of oak pollens in the field using our mobile device. In the Spring of 2018, we used our instrument to measure bio-aerosols in air close to a line of four oak trees (Quercus Virginiana) at the University of California, Los Angeles campus [55]. A three-minute air sample is taken close to these trees at a pumping rate of 13 L / min, as illustrated in Figure 5(a). The whole FOV reconstruction of this sample is shown in Figure 5(b), which also highlights different ROIs corresponding to the oak tree pollens automatically detected by our deep learning-based algorithm. In these 12 ROIs, there are two false positive detections (Figure 5(b-1) and Figure 5(b-5)), which are actually plant fragments that have elongated shapes. Similar mis-classifications of the CNN that classifies plant fragments as pollens also happened for the other two pollens – Bermuda grass and ragweed, as shown in Figure S5. This problem might be addressed in the future by including such plant fragment images in our training dataset as an additional label.

We also examined the entire FOV to screen for the false negative detections of oak tree pollens. Of all the detected bio-aerosols, we see that the CNN missed one cluster of oak tree pollens within the FOV, as marked by a blue rectangle in Figure 5(b) and shown in Figure 5(c), which is classified as Bermuda with a high score. From Figure 5(c), we see that this image contains two oak tree pollens clustered together, and since the training dataset only included isolated oak tree pollens it was misclassified as a Bermuda grass pollen, which is generally larger in size and rounder in shape than an oak tree pollen (providing a better fit to a cluster of oak pollens). Although the occurrence of clustered pollens is relatively rare, these types of misclassifications can be reduced by including clusters of pollen examples in our training dataset, or using per-pixel semantic segmentation instead of a classification CNN.

CONCLUSION

In summary, our mobile bio-aerosol sensing platform is hand-held, cost-effective and accurate. We believe that it can be used to build a wide-coverage automated bio-aerosol monitoring network in a cost-effective and scalable manner, which can rapidly provide accurate response for spatio-temporal mapping of bio-aerosol concentrations. Our device is controlled wirelessly and can potentially be carried by unmanned vehicles such as drones to access bio-aerosol monitoring sites that may be dangerous for human inspectors.

METHODS

Computational-imaging-based bio-aerosol monitoring

To perform label-free sensing of bio-aerosols, a computational air quality monitor based on lens-less microscopy is developed. Figure 1(a) shows its design schematics. It contains a miniaturized vacuum pump (M00198, GTEK Automation) that takes in air through a disposable impactor (Air-O-Cell Sampling Cassette, Zefon International, Inc.) at 13 L/min. The impactor has a sticky polymer coverslip right below the impactor nozzle with a spacing of ~ 800 μm between them (Figure 1(b)). Because of their larger momentum, aerosols and bio-aerosols within the input air stream cannot follow the output air path, so they hit on and are collected by the sticky coverslip of our impactor. An infrared vertical-cavity surface-emitting laser (VCSEL) diode (OPV300, TT Electronics, $\lambda_p = 850\,nm$) illuminates the collected aerosols from above, casting an in-line hologram of the samples, which is recorded by a complementary metal–oxide–semiconductor (CMOS) image sensor chip (Sony IMX219PQ, pixel pitch 1.12 μm). These in-line holograms are sent to a remote server (e.g., a local PC) where the aerosol images are analyzed automatically, as will be detailed in the subsequent sections. To avoid secondary light sources from the reflection and refraction of the transparent impactor nozzle, a 3D-printed black cover is used to tightly cover the impactor surface.

A driver chip (TLC5941NT, Texas Instruments) controls the current of our illumination VCSEL at its threshold (3 mA), which provides adequate coherence without introducing speckle noise. 850 nm illumination wavelength is specifically chosen to use all of the four Bayer channels on the color CMOS imager, since all the four Bayer channels have equal transmission at this wavelength, making it function like a monochrome sensor for our holographic imaging purposes (see Figure S6 for details). Benefited from this, as well as higher coherence of the laser diode, a better spatial resolution is achieved (see the Results and Figure S1 for details). Our entire mobile device is powered by a Lithium polymer (Li-po) battery (Turnigy Nano-tech 1000mAh 4S 45~90C Li-po pack) and controlled by an embedded single board computer (Raspberry Pi Zero W).

Simultaneous autofocusing and phase recovery of bio-aerosols using deep learning

To simultaneously perform digital autofocusing and phase recovery for each individual aerosol, a CNN-based method is used [43], built using Tensorflow [56]. This CNN is trained with pairs of defocused back-propagated holograms and their corresponding in-focus, phase recovered images (ground truth, GT images). These phase recovered GT images are generated using a multi-height phase recovery algorithm [57] using eight hologram measurements at different sample-to-sensor distances. After its training, the CNN can perform autofocusing and phase recovery for each individual aerosol in our imaging FOV, all in parallel (up to a defocus distance of ± 100 μm), and rapidly generates a phase-recovered, extended DOF reconstruction of the image FOV. Due to limited graphical memory of our computer, the full FOV back-propagated image (9840 × 3069 × 2) cannot be processed directly; it is therefore divided into 12-by-5 patches of 1024-by-1024 pixels with a spatial overlap of 100-pixels between images. Each individual patch is processed in sequence and the results are combined after this reconstruction step to reveal the bio-aerosol distribution captured within the entire FOV. Each patch takes ~ 0.4 s to process, totaling ~ 25 s for the entire FOV.

Aerosol detection algorithm

A multi-scale spot detection algorithm similar to Ref. [58] is developed to detect and extract each aerosol ROI (see Supplementary Material and Figure S7(a) for details). This algorithm takes six levels of high pass filtering of the complex amplitude image per ROI, obtained by the difference of the original image and the blurred images filtered by six different kernels. These high-passed images are per-pixel multiplied with each other to obtain a correlation image. A binary mask is then obtained by thresholding this correlation image with three-times the standard deviation added to the mean of the correlation image. This binary mask is dilated by 11 pixels, and the connected components are used to estimate a circle with the centroid and radius of each one of the detected spots, which marks the location and rough size of each detected bio-aerosol. To avoid multiple detections of the same aerosol, a non-maximum suppression criterion is applied, where if an estimated circle has more than 10% of overlapping area with another circle, only the bigger one is considered/counted. The resulting centroids are cropped into 256×256 pixel ROIs, which are then fed into the bio-aerosol classification CNN, detailed in the next sub-section. This algorithm takes < 5 s for the whole FOV, and achieves better performance compared to conventional circle detection algorithms such as circular Hough transform [59], achieving 98.4% detection precision and 92.5% detection recall, as detailed in Figure S7(b).

Deep learning-based classification of bio-aerosols

The classification CNN architecture is shown in the zoom-in part of Figure 2(b), which is inspired by ResNet [60]. The network contains five residual blocks, where each block maps the input tensor x_k into output tensor x_{k+1}, for a given block k ($k = 1,2,3,4,5$), i.e.,

$$\mathrm{x'_k} = \mathrm{x_k} + \mathrm{ReLU}\left[\mathrm{CONV_{k_1}}\left\{\mathrm{ReLU}\left[\mathrm{CONV_{k_1}}\{\mathrm{x_k}\}\right]\right\}\right] \quad (4)$$

$$\mathrm{x_{k+1}} = \mathrm{MAX}\left(\mathrm{x'_k} + \mathrm{ReLU}\left[\mathrm{CONV_{k_2}}\left\{\mathrm{ReLU}\left[\mathrm{CONV_{k_1}}\{\mathrm{x'_k}\}\right]\right\}\right]\right) \quad (5)$$

where ReLU stands for rectified linear unit operation, CONV stands for the convolution operator (including the bias terms), and MAX stands for the max-pooling operator. The subscript k_1 and k_2 denote the number of channels in the corresponding convolution layer, where k_1 equals to the number of input channels and k_2 expands the number of channels twice, i.e. $k_1 = 16, 32, 64, 128, 256$ and $k_2 = 32, 64, 128, 256, 512$ for each residual block ($k = 1,2,3,4,5$). Zero padding is used on the tensor $\mathrm{x'_k}$ to compensate the mismatch between the number of input and output channels. All the convolutional layers use a convolutional kernel of 3×3 pixels, a stride of one pixel, and a replicate-padding of one pixel. All the max-pooling layers use a kernel of two pixels, and a stride of two pixels, which reduces the width and height of the image by half.

Following the residual blocks, an average pooling layer reduces the width and height of the tensor to one, which is followed by a fully-connected (FC) layer of size 512×512. Dropout with 0.5 probability is used on this FC layer to increase performance and prevent overfitting. Another fully connected layer of size 512×6 maps the 512 channels to 6 class scores for final determination of the class of each bio-aerosol that is imaged by our device.

During training, the network minimizes the soft-max cross-entropy loss between the true label and the output scores:

$$L = \sum_i \left[-\log\left(\frac{e^{f_{y_i}(x_i)}}{\sum_j e^{f_j(x_i)}}\right)\right] \quad (6)$$

where $\mathrm{f_j}(x_i)$ is the class score for the class j given input data $\mathrm{x_i}$, and $\mathrm{y_i}$ is the corresponding true class for $\mathrm{x_i}$. The dataset contains ~ 1,500 individual 256×256 pixel ROIs for each of the six classes, totaling ~10,000 images. 70% of the data for each class is randomly selected for training, and remaining images are equally divided to validation and testing sets. The training takes ~ 2 h for 200 epochs. The best trained model is selected to be the one that gives lowest soft-max loss for the validation set within 200 training epochs. The testing takes < 0.02 s for each 256×256 pixel ROI. For a typical FOV with e.g., ~ 500 particles, this step is completed in ~10 s. For additional details on the overall

image processing time budget, please refer to Supplementary Material.

ASSOCIATED CONTENT

Supplementary Material

Additional methods: Shade correction and differential holographic imaging. Digital holographic reconstruction of differential holograms. Comparison of our deep learning classification results against SVM and AlexNet. Spot detection algorithm for bio-aerosol localization. Bio-aerosol sampling experiments in the lab. Bio-aerosol sample preparation.
Additional discussions: Using deep learning in label-free bio-aerosol sensing. Detailed comparison of this work with some recent learning-based bio-aerosol detection methods. Image acquisition and data processing time. Future work.
Supplementary figures: Resolution test using a USAF 1951 test-target. Full-FOV reconstruction. Confusion matrices for bio-aerosol mixture experiments. Examples of cropped regions with more than one type of bio-aerosols per zoomed FOV. False positive detections of Bermuda grass and ragweed pollens in the oak tree pollen field testing. Sensor response of Sony IMX219PQ. Bio-aerosol localization using a spot-detection algorithm. Experimental setup for bio-aerosol sensing in the lab.

AUTHOR INFORMATION

Corresponding Author Email: ozcan@ucla.edu

ORCID

Yichen Wu: 0000-0002-9343-5489

Aydogan Ozcan: 0000-0002-0717-683X

Author Contributions

A.O. and Y.W. conceived the research, Y.W. and A.C. prepared the samples. Y.W., A.C., and Y.L. performed the aerosol sampling experiments. A.C. did the manual inspection and labeling of bio-aerosols. Y.W., Y.L., C.C., M.L., Y.R., and X.L. processed the data. A.O., Y.W., A.C., and Y.L. prepared the manuscript. H.C.K., Y.Z., H.W., and Z.G. contributed to experiments. A.O. initiated and supervised the research.

FUNDING SOURCES

National Science Foundation (NSF); NSF Partnerships for Innovation: Building Innovation Capacity (PFI:BIC) Program; Vodafone Americas Foundation; Howard Hughes Medical Institute.

ACKNOWLEDGMENT

The authors acknowledge the Aerobiology Laboratory Association, Inc. in Huntington Beach, CA for providing some of the experiment materials. Derek Tseng of UCLA is also acknowledged for his help with the table of contents image.

REFERENCES

(1) Aimanianda, V.; Bayry, J.; Bozza, S.; Kniemeyer, O.; Perruccio, K.; Elluru, S. R.; Clavaud, C.; Paris, S.; Brakhage, A. A.; Kaveri, S. V.; et al. Surface Hydrophobin Prevents Immune Recognition of Airborne Fungal Spores. *Nature* **2009**, *460*, 1117-U79.

(2) Srikanth, P.; Sudharsanam, S.; Steinberg, R. Bio-Aerosols in Indoor Environment: Composition, Health Effects and Analysis. *Indian Journal of Medical Microbiology* **2008**, *26*, 302.

(3) Codina, R.; Fox, R. W.; Lockey, R. F.; DeMarco, P.; Bagg, A. Typical Levels of Airborne Fungal Spores in Houses without Obvious Moisture Problems during a Rainy Season in Florida, USA. *J Investig Allergol Clin Immunol* **2008**, *18*, 156–162.

(4) de Ana, S. G.; Torres-Rodríguez, J. M.; Ramírez, E. A.; García, S. M.; Belmonte-Soler, J. Seasonal Distribution of Alternaria, Aspergillus, Cladosporium and Penicillium Species Isolated in Homes of Fungal Allergic Patients. *J Investig Allergol Clin Immunol* **2006**, *16*, 357–363.

(5) Lee, T.; Grinshpun, S. A.; Martuzevicius, D.; Adhikari, A.; Crawford, C. M.; Reponen, T. Culturability and Concentration of Indoor and Outdoor Airborne Fungi in Six Single-Family Homes. *Atmos Environ* **2006**, *40*, 2902–2910.

(6) Douglas, P.; Robertson, S.; Gay, R.; Hansell, A. L.; Gant, T. W. A Systematic Review of the Public Health Risks of Bioaerosols from Intensive Farming. *International Journal of Hygiene and Environmental Health* **2018**, *221*, 134–173.

(7) Kim, K.-H.; Kabir, E.; Jahan, S. A. Airborne Bioaerosols and Their Impact on Human Health. *Journal of Environmental Sciences* **2018**, *67*, 23–35.

(8) Fischer, G.; Albrecht, A.; Jäckel, U.; Kämpfer, P. Analysis of Airborne Microorganisms, MVOC and Odour in the Surrounding of Composting Facilities and Implications for Future Investigations. *International Journal of Hygiene and Environmental Health* **2008**, *211*, 132–142.

(9) Hryhorczuk, D.; Curtis, L.; Scheff, P.; Chung, J.; Rizzo, M.; Lewis, C.; Keys, N.; Moomey, M. Bioaerosol Emissions from a Suburban Yard Waste Composting Facility. *Ann Agric Environ Med* **2001**, *8*, 177–185.

(10) Pearson, C.; Littlewood, E.; Douglas, P.; Robertson, S.; Gant, T. W.; Hansell, A. L. Exposures and Health Outcomes in Relation to Bioaerosol Emissions From Composting Facilities: A Systematic Review of Occupational and Community Studies. *J Toxicol Environ Health B Crit Rev* **2015**, *18*, 43–69.

(11) D'Amato, G.; Cecchi, L.; Bonini, S.; Nunes, C.; Annesi□ Maesano, I.; Behrendt, H.; Liccardi, G.; Popov, T.; Cauwenberge, P. V. Allergenic Pollen and Pollen Allergy in Europe. *Allergy 62*, 976–990.

(12) Dedesko, S.; Stephens, B.; Gilbert, J. A.; Siegel, J. A. Methods to Assess Human Occupancy and Occupant Activity in Hospital Patient Rooms. *Building and Environment* **2015**, *90*, 136–145.

(13) WHO, Ambient (outdoor) air quality and health http://www.who.int/mediacentre/factsheets/fs313/en/ (accessed May 28, 2016).

(14) Samet, J.; Saldiva, P. H. N.; Brauer, M.; Chen, G.; White, P.; Huang, W.; Knudsen, L. E.; Møller, P.; Raaschou-Nielsen, O.; Forastiere, F.; et al. The Carcinogenicity of Outdoor Air Pollution. *Res Rep Health Eff Inst* **2009**, *140*, 5–114.

(15) Walt, D. R.; Franz, D. R. Peer Reviewed: Biological Warfare Detection. *Analytical chemistry* **2000**, *72*, 738–A.

(16) Mandal, J.; Brandl, H. Bioaerosols in Indoor Environment - A Review with Special Reference to Residential

and Occupational Locations. *The Open Environmental & Biological Monitoring Journal* **2011**, *4*, 83-96.

(17) Usachev, E. V.; Tam, A. M.; Usacheva, O. V.; Agranovski, I. E. The Sensitivity of Surface Plasmon Resonance Based Viral Aerosol Detection. *Journal of Aerosol Science* **2014**, *76*, 39–47.

(18) Halsby, K. D.; Kirkbride, H.; Walsh, A. L.; Okereke, E.; Brooks, T.; Donati, M.; Morgan, D. The Epidemiology of Q Fever in England and Wales 2000–2015. *Vet Sci* **2017**, *4*, E28.

(19) Haig, C. W.; Mackay, W. G.; Walker, J. T.; Williams, C. Bioaerosol Sampling: Sampling Mechanisms, Bioefficiency and Field Studies. *J. Hosp. Infect.* **2016**, *93*, 242–255.

(20) Wu, Y.; Shen, F.; Yao, M. Use of Gelatin Filter and BioSampler in Detecting Airborne H5N1 Nucleotides, Bacteria and Allergens. *Journal of Aerosol Science* **2010**, *41*, 869–879.

(21) Rodriguez-Riano, T.; Dafni, A. A New Procedure to Asses Pollen Viability. *Sex Plant Reprod* **2000**, *12*, 241–244.

(22) Heslop-Harrison, J.; Heslop-Harrison, Y. Evaluation of Pollen Viability by Enzymatically Induced Fluorescence; Intracellular Hydrolysis of Fluorescein Diacetate. *Stain Technol* **1970**, *45*, 115–120.

(23) National Allergy Forecast & Info About Allergies | Pollen.com https://www.pollen.com/ (accessed Jun 1, 2018).

(24) Kaye, P. H.; Stanley, W. R.; Hirst, E.; Foot, E. V.; Baxter, K. L.; Barrington, S. J. Single Particle Multichannel Bio-Aerosol Fluorescence Sensor. *Opt. Express* **2005**, *13*, 3583–3593.

(25) Reyes, F. L.; Jeys, T. H.; Newbury, N. R.; Primmerman, C. A.; Rowe, G. S.; Sanchez, A. Bio-Aerosol Fluorescence Sensor. *Field Analytical Chemistry & Technology* **1999**, *3*, 240–248.

(26) Eversole, J. D.; Hardgrove, J. J.; Cary, W. K.; Choulas, D. P.; Seaver, M. Continuous, Rapid Biological Aerosol Detection with the Use of UV Fluorescence: Outdoor Test Results. *Field Anal. Chem. Technol.* **1999**, *3*, 249–259.

(27) Ruske, S.; Topping, D. O.; Foot, V. E.; Kaye, P. H.; Stanley, W. R.; Crawford, I.; Morse, A. P.; Gallagher, M. W. Evaluation of Machine Learning Algorithms for Classification of Primary Biological Aerosol Using a New UV-LIF Spectrometer. *Atmos. Meas. Tech.* **2017**, *10*, 695–708.

(28) Leśkiewicz, M.; Kaliszewski, M.; Włodarski, M.; Młyńczak, J.; Mierczyk, Z.; Kopczyński, K. Improved Real-Time Bio-Aerosol Classification Using Artificial Neural Networks. *Atmospheric Measurement Techniques Discussions* **2018**, 1–19.

(29) Johnson, B. N.; Mutharasan, R. Biosensing Using Dynamic-Mode Cantilever Sensors: A Review. *Biosensors and Bioelectronics* **2012**, *32*, 1–18.

(30) Kovář, D.; Farka, Z.; Skládal, P. Detection of Aerosolized Biological Agents Using the Piezoelectric Immunosensor. *Anal. Chem.* **2014**, *86* , 8680–8686.

(31) Usachev, E. V.; Usacheva, O. V.; Agranovski, I. E. Surface Plasmon Resonance-Based Real-Time Bioaerosol Detection. *J. Appl. Microbiol.* **2013**, *115*, 766–773.

(32) Schwarzmeier, K.; Knauer, M.; Ivleva, N. P.; Niessner, R.; Haisch, C. Bioaerosol Analysis Based on a Label-Free Microarray Readout Method Using Surface-Enhanced Raman Scattering. *Anal Bioanal Chem* **2013**, *405*, 5387–5392.

(33) Grow, A. E.; Wood, L. L.; Claycomb, J. L.; Thompson, P. A. New Biochip Technology for Label-Free Detection of Pathogens and Their Toxins. *Journal of Microbiological Methods* **2003**, *53*, 221–233.

(34) DeAngelis, K. M.; Wu, C. H.; Beller, H. R.; Brodie, E. L.; Chakraborty, R.; DeSantis, T. Z.; Fortney, J. L.; Hazen, T. C.; Osman, S. R.; Singer, M. E.; et al. PCR Amplification-Independent Methods for Detection of Microbial Communities by the High-Density Microarray PhyloChip ?. *Appl Environ Microbiol* **2011**, *77*, 6313–6322.

(35) Verma, J.; Saxena, S.; Babu, S. G. ELISA-Based Identification and Detection of Microbes. In *Analyzing Microbes*; Springer Protocols Handbooks; Springer, Berlin, Heidelberg, 2013; pp 169–186.

(36) Cha, S.; Srinivasan, S.; Jang, J. H.; Lee, D.; Lim, S.; Kim, K. S.; Jheong, W.; Lee, D.-W.; Park, E.-R.; Chung, H.-M.; et al. Metagenomic Analysis of Airborne Bacterial Community and Diversity in Seoul, Korea, during December 2014, Asian Dust Event. *PLOS ONE* **2017**, *12*, e0170693.

(37) Thomas, T.; Gilbert, J.; Meyer, F. Metagenomics - a Guide from Sampling to Data Analysis. *Microb Inform Exp* **2012**, *2*, 3.

(38) Wu, Y.-C.; Shiledar, A.; Li, Y.-C.; Wong, J.; Feng, S.; Chen, X.; Chen, C.; Jin, K.; Janamian, S.; Yang, Z.; et al. Air Quality Monitoring Using Mobile Microscopy and Machine Learning. *Light: Science & Applications* **2017**, *6*, e17046.

(39) Wu, Y.; Ozcan, A. Lensless Digital Holographic Microscopy and Its Applications in Biomedicine and Environmental Monitoring. *Methods* **2018**, *136*, 4–16.

(40) Greenbaum, A.; Luo, W.; Su, T.-W.; Göröcs, Z.; Xue, L.; Isikman, S. O.; Coskun, A. F.; Mudanyali, O.; Ozcan, A. Imaging without Lenses: Achievements and Remaining Challenges of Wide-Field on-Chip Microscopy. *Nature methods* **2012**, *9*, 889–895.

(41) Bianco, V.; Mandracchia, B.; Marchesano, V.; Pagliarulo, V.; Olivieri, F.; Coppola, S.; Paturzo, M.; Ferraro, P. Endowing a Plain Fluidic Chip with Micro-Optics: A Holographic Microscope Slide. *Light: Science & Applications* **2017**, *6*, e17055.

(42) Mandracchia, B.; Bianco, V.; Wang, Z.; Mugnano, M.; Bramanti, A.; Paturzo, M.; Ferraro, P. Holographic Microscope Slide in a Spatio-Temporal Imaging Modality for Reliable 3D Cell Counting. *Lab Chip* **2017**, *17*, 2831–2838.

(43) Wu, Y.; Rivenson, Y.; Zhang, Y.; Wei, Z.; Günaydin, H.; Lin, X.; Ozcan, A. Extended Depth-of-Field in Holographic Imaging Using Deep-Learning-Based Autofocusing and Phase Recovery. *Optica, OPTICA* **2018**, *5*, 704–710.

(44) Solomon, W. R.; Burge, H. A.; Muilenberg, M. L. Allergen Carriage by Atmospheric Aerosol. I. Ragweed Pollen Determinants in Smaller Micronic Fractions. *J. Allergy Clin. Immunol.* **1983**, *72*, 443–447.

(45) Habenicht, H. A.; Burge, H. A.; Muilenberg, M. L.; Solomon, W. R. Allergen Carriage by Atmospheric Aerosol: II. Ragweed-Pollen Determinants in Submicronic Atmospheric Fractions. *Journal of Allergy and Clinical Immunology* **1984**, *74*, 64–67.

(46) Fernandez-Caldas, E.; Swanson, M. C.; Pravda, J.; Welsh, P.; Yunginger, J. W.; Reed, C. E. Immunochemical Demonstration of Red Oak Pollen Aeroallergens Outside the Oak Pollination Season. *Grana* **1989**, *28*, 205–209.

(47) Bishara, W.; Sikora, U.; Mudanyali, O.; Su, T.-W.; Yaglidere, O.; Luckhart, S.; Ozcan, A. Holographic Pixel Super-Resolution in Portable Lensless on-Chip Micros-

copy Using a Fiber-Optic Array. *Lab on a Chip* **2011**, *11*, 1276–1279.

(48) Wu, Y.; Zhang, Y.; Luo, W.; Ozcan, A. Demosaiced Pixel Super-Resolution for Multiplexed Holographic Color Imaging. *Sci Rep* **2016**, *6,* 28601.

(49) Luo, W.; Zhang, Y.; Feizi, A.; Gorocs, Z.; Ozcan, A. Pixel Super-Resolution Using Wavelength Scanning. *Light: Science & Applications* **2016**, *5*, e16058.

(50) Su, T.-W.; Erlinger, A.; Tseng, D.; Ozcan, A. Compact and Light-Weight Automated Semen Analysis Platform Using Lensfree on-Chip Microscopy. *Analytical chemistry* **2010**, *82*, 8307–8312.

(51) Miccio, L.; Finizio, A.; Puglisi, R.; Balduzzi, D.; Galli, A.; Ferraro, P. Dynamic DIC by Digital Holography Microscopy for Enhancing Phase-Contrast Visualization. *Biomed. Opt. Express, BOE* **2011**, *2*, 331–344.

(52) Krizhevsky, A.; Sutskever, I.; Hinton, G. E. ImageNet Classification with Deep Convolutional Neural Networks. In *Advances in Neural Information Processing Systems 25*; Pereira, F., Burges, C. J. C., Bottou, L., Weinberger, K. Q., Eds.; Curran Associates, Inc., 2012; pp 1097–1105.

(53) Bishop, C. *Pattern Recognition and Machine Learning (Information Science and Statistics), 1st Edn. 2006. Corr. 2nd Printing Edn*; Springer, New York, 2007.

(54) Ronneberger, O.; Fischer, P.; Brox, T. U-Net: Convolutional Networks for Biomedical Image Segmentation. *arXiv:1505.04597 [cs]* **2015**.

(55) CampusPlantsSearchResults – Mildred E. Mathias Botanical Garden. https://www.botgard.ucla.edu/ (accessed Jun 4, 2018).

(56) Abadi, M.; Barham, P.; Chen, J.; Chen, Z.; Davis, A.; Dean, J.; Devin, M.; Ghemawat, S.; Irving, G.; Isard, M. TensorFlow: A System for Large-Scale Machine Learning. In *OSDI*; 2016; Vol. 16, pp 265–283.

(57) Greenbaum, A.; Ozcan, A. Maskless Imaging of Dense Samples Using Pixel Super-Resolution Based Multi-Height Lensfree on-Chip Microscopy. *Optics express* **2012**, *20*, 3129–3143.

(58) Olivo-Marin, J.-C. Extraction of Spots in Biological Images Using Multiscale Products. *Pattern Recognition* **2002**, *35*, 1989–1996.

(59) Xu, L.; Oja, E.; Kultanen, P. A New Curve Detection Method: Randomized Hough Transform (RHT). *Pattern Recognition Letters* **1990**, *11*, 331–338.

(60) He, K.; Zhang, X.; Ren, S.; Sun, J. Deep Residual Learning for Image Recognition; 2016; pp 770–778.

FIGURES AND CAPTIONS

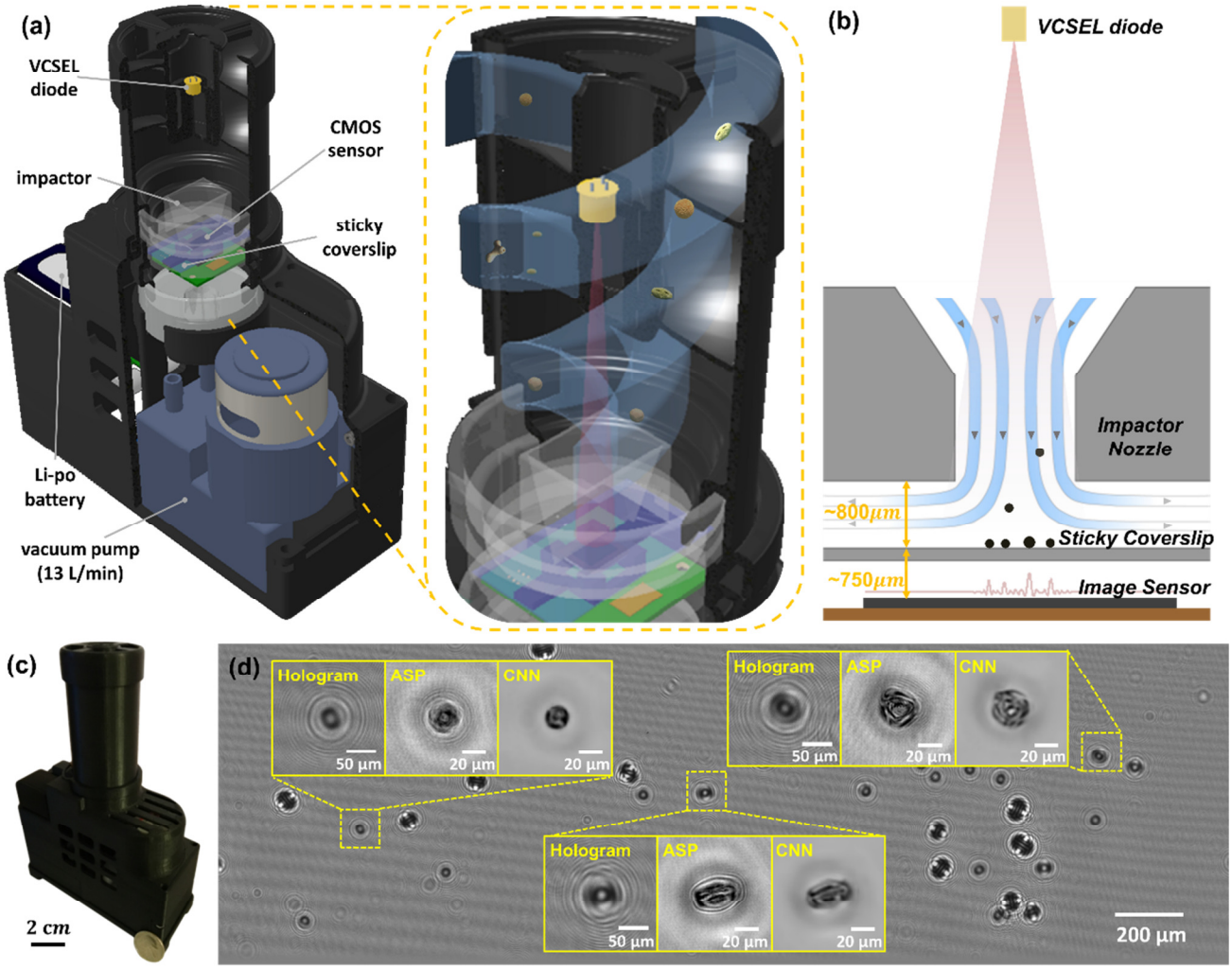

Figure 1. Label-free bio-aerosol sensing device. (a) 3D computer-aided-design (CAD)-drawing overview of our device. (b) Schematic drawing of impaction-based air sampling on a chip. (c) A photo of the device. A quarter coin is placed next to the device for providing the relative scale of our instrument. (d) Whole FOV differential hologram of a bio-aerosol sample, with zoomed-in regions showing the raw hologram, its angular spectrum-based back-propagated image (ASP) and a CNN-based reconstructed image.

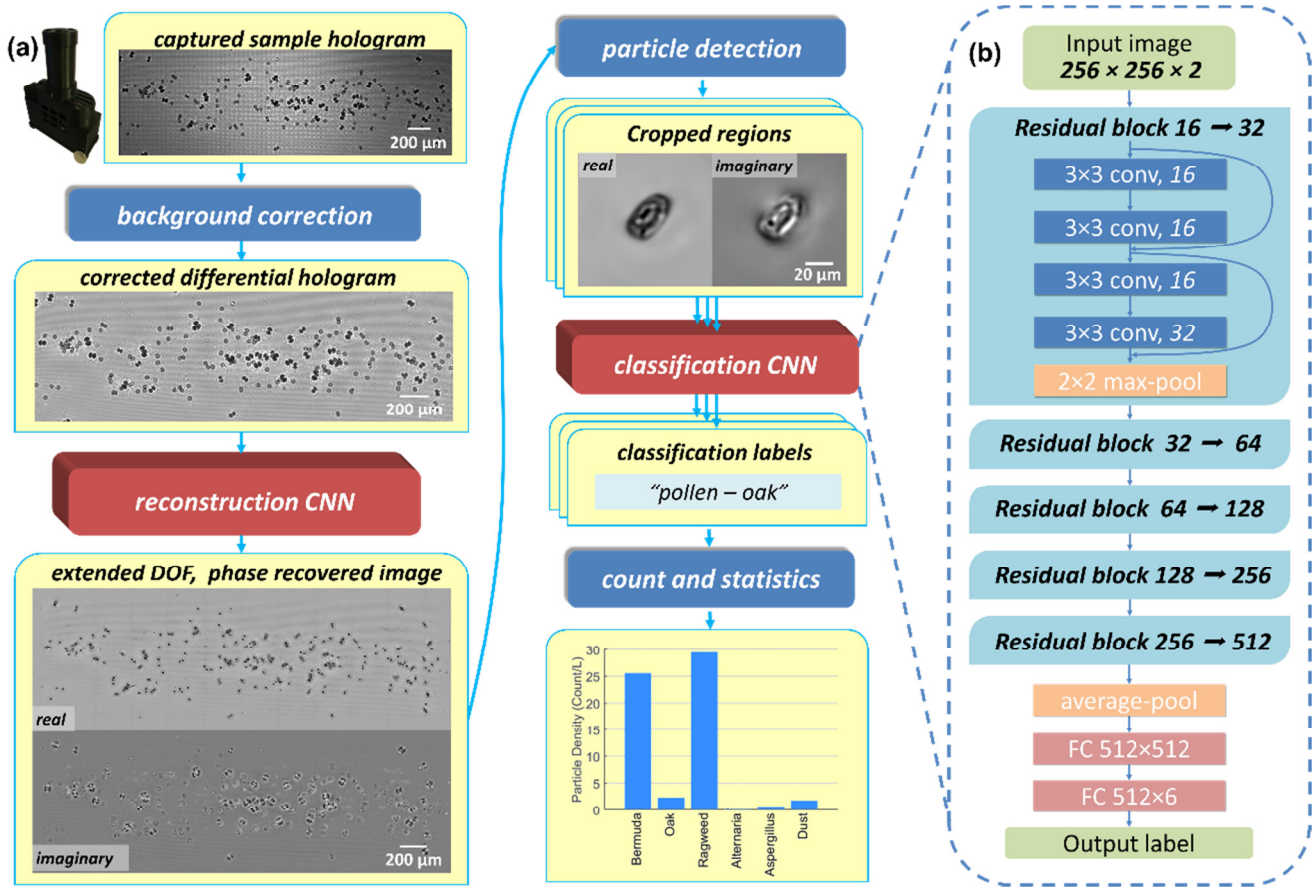

Figure 2. Label-free bio-aerosol sensing. (a) Our image reconstruction and bio-aerosol classification work-flow. (b) Architecture of the classification CNN. conv: convolutional layer. FC: fully-connected layer.

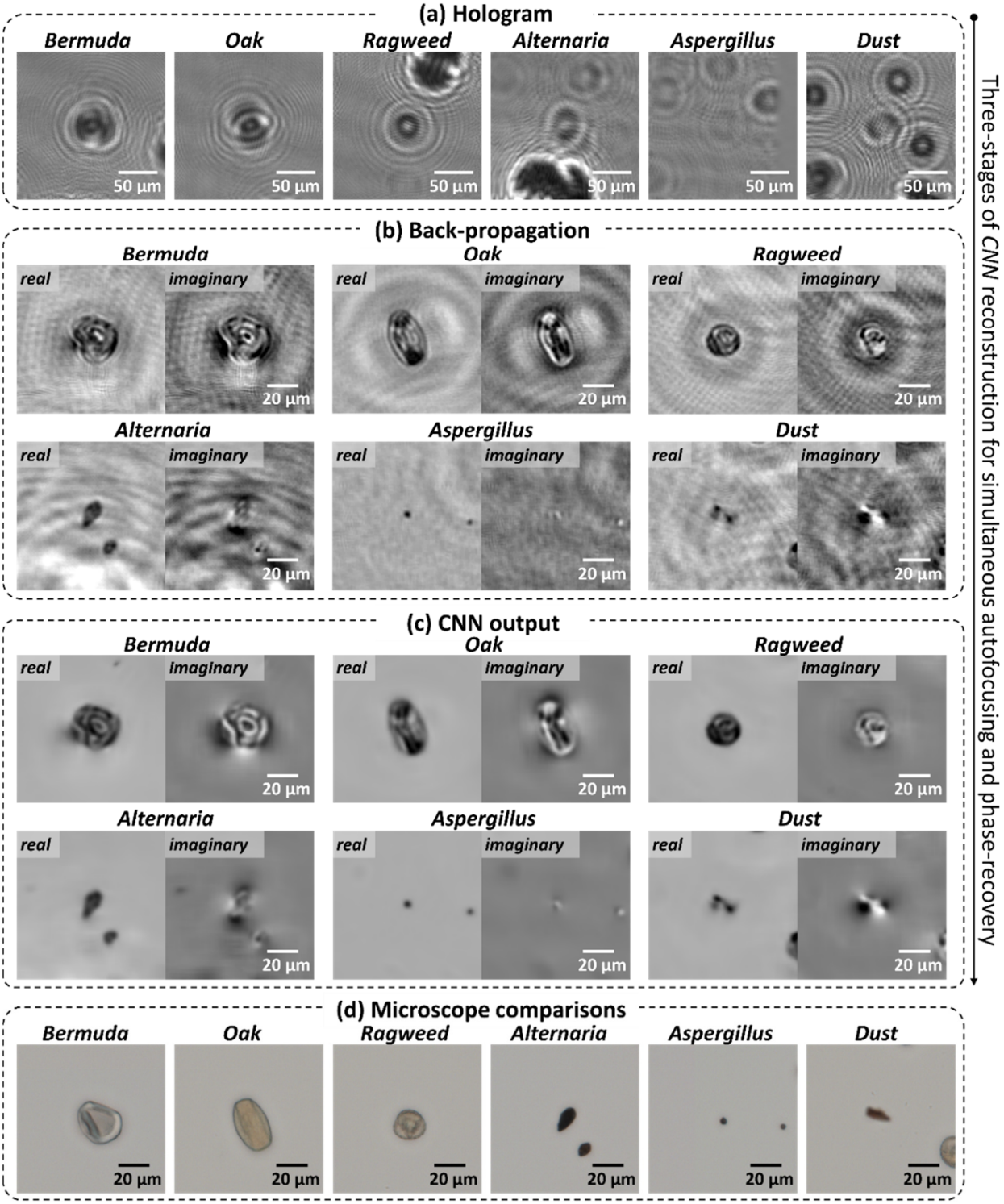

Figure 3. Examples of the reconstructed images of different types of bio-aerosols. (a) Cropped raw hologram. (b) Back-propagated holographic reconstruction. (c) CNN-based hologram reconstruction. (d) Corresponding regions of interest imaged by a benchtop scanning microscope with 40× magnification.

	This paper			*AlexNet*			*SVM*		
	Preci.	**Recall**	**F#**	**Preci.**	**Recall**	**F#**	**Preci.**	**Recall**	**F#**
Bermuda	0.925287	0.851852	0.887052	0.893855	0.846561	0.869565	0.769231	0.61674	0.684597
Oak	0.930464	0.975694	0.952542	0.940972	0.940972	0.940972	0.84375	0.690341	0.759375
Ragweed	0.964427	0.976	0.970179	0.931559	0.98	0.955166	0.730077	0.8875	0.801128
Alternaria	0.962963	0.962963	0.962963	0.933333	0.972222	0.952381	0.587179	0.970339	0.731629
Aspergillus	0.848485	0.937799	0.890909	0.795556	0.856459	0.824885	0.782222	0.671756	0.722793
Dust	0.944186	0.849372	0.894273	0.843602	0.74477	0.791111	0.833333	0.6	0.697674
Average	0.940059	0.934515	0.936591	0.922129	0.922511	0.921901	0.781019	0.731527	0.748367

Table. 1. Precision and recall of our bio-aerosol classification results using a convolutional neural network. Comparison of our neural network against two other machine learning methods, AlexNet [52] and support vector machine (SVM) [53], is also provided.

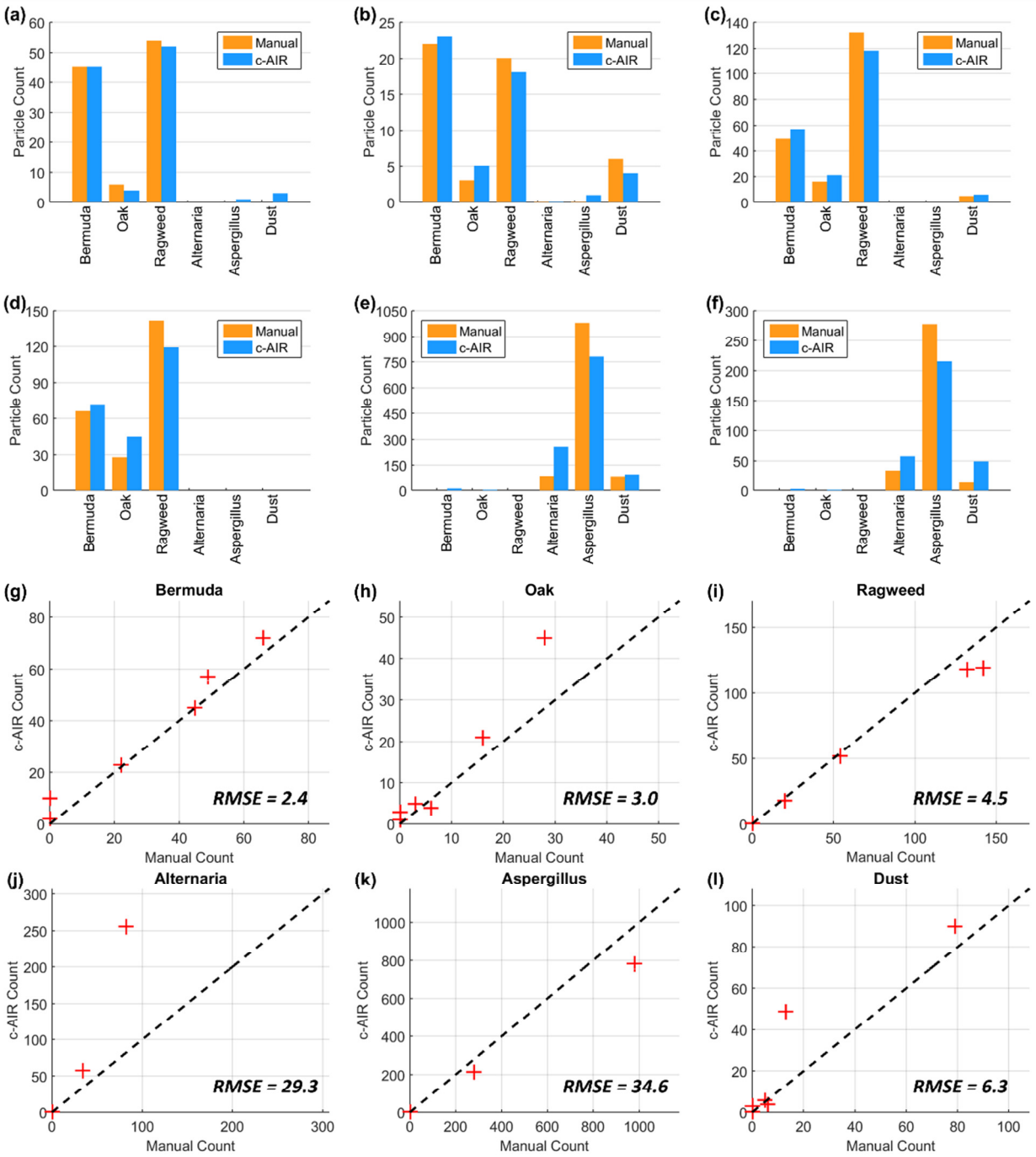

Figure 4. Bio-aerosol mixture experiments. (a-f) Deep-learning based automatic bio-aerosol detection and counting using our mobile device for six different experiments with varying bio-aerosol concentrations, and their comparisons against manual counting performed by a microbiologist under a benchtop scanning microscope with 40× magnification are shown. (g-l) Quantification of our counting accuracy for different types of aerosols. The dashed line refers to y = x. Root mean square error (RMSE) is also shown in each sub-figure.

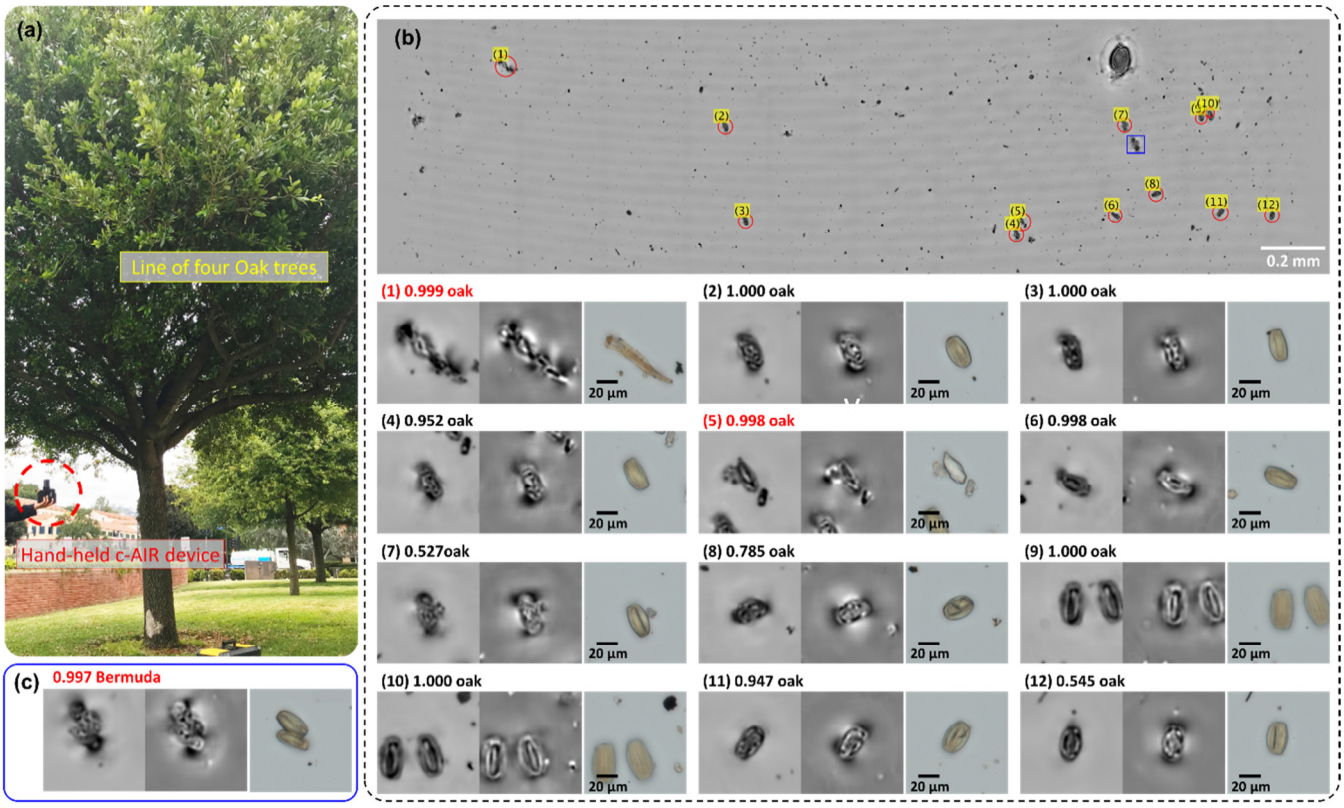

Figure 5. Sensing of oak tree pollens in the field. (a) Field testing of our mobile bio-aerosol sensing device is performed under a line of four oak trees in Los Angeles (Spring of 2018). (b) Full-FOV reconstruction of the captured aerosol samples is shown, where the oak pollen bio-aerosols that are detected by our deep learning-based classification algorithm are marked by red circles. The zoomed-in images of these detected particles, with real (left) and imaginary (right) images, reconstructed also using a deep neural network, are shown in (1) – (12). A comparison image captured later using a benchtop microscope under 40× magnification is also shown for each region. Softmax classification scores for each captured aerosol are also shown on top of each ROI. The two misclassification cases, (1) and (5), are marked in red. (c) A cluster of oak particles is misclassified as Bermuda pollen. Its location is highlighted by a blue square in (b).

Label-free bio-aerosol sensing using mobile microscopy and deep learning

Yichen Wu,[1,2,3] Ayfer Calis,[1,2,3] Yi Luo,[1,2,3] Cheng Chen,[1] Maxwell Lutton,[4] Yair Rivenson,[1,2,3] Xing Lin,[1,2,3] Hatice Ceylan Koydemir,[1,2,3] Yibo Zhang,[1,2,3] Hongda Wang,[1,2,3] Zoltán Görücs,[1,2,3] Aydogan Ozcan,[1,2,3,5*]

[1]Electrical and Computer Engineering Department, University of California, Los Angeles, California 90095, USA

[2]Bioengineering Department, University of California, Los Angeles, California 90095, USA

[3]California NanoSystems Institute (CNSI), University of California, Los Angeles, California 90095, USA

[4]Computer Science Department, University of California, Los Angeles, California 90095, USA

[5]Department of Surgery, David Geffen School of Medicine, University of California, Los Angeles, California 90095, USA

[*]Corresponding author: ozcan@ucla.edu

Table of contents figure & brief synopsis:

We report a portable and cost-effective holographic device that rapidly screens air at a throughput of 13 L/min, and automatically reconstructs microscopic images of individual bio-aerosols to perform label-free sensing and classification of these bio-aerosols using deep learning.